Journal of Materials Chemistry C

ROYAL SOCIETY OF CHEMISTRY

PAPER

View Article Online
View Journal

Cite this: DOI: 10.1039/d6tc00519e

One-step decomposition pathway for solution-derived metal oxide layers driven by hydroxyl radical atmospheres

Y. A. Rivas,[a] M. Echaniz-Cintora,[a] A. Barreto,[ad] J. A. Molina-Calzada,[bc] J. A. Vidal-Moya,[e] M. C. Serrano,[a] R. Jiménez,[a] Í. Bretos[a] and M. L. Calzada *[a]

Received 17th February 2026,
Accepted 12th May 2026

DOI: 10.1039/d6tc00519e

rsc.li/materials-c

Solution deposition of high-performance oxide films has attracted intense research interest driven by the need for sustainable synthesis strategies that simplify key processes such as ligand removal, oxidation of organic residues, and the formation of amorphous and crystalline oxide phases. These approaches aim not only to reduce the carbon footprint but also to lower the thermal budget required for oxide film formation, thereby enabling direct, large-area deposition on low-cost, temperature-sensitive substrates required for emerging applications in thin-film electronics. In this work, we elucidate the chemical mechanism underlying the crystallization of solution-processed metal oxide films under highly reactive hydroxyl (•OH) radical atmospheres. These radicals promote a simple, rapid, one-step decomposition of solution-derived films, directly yielding crystalline oxide films with substantially reduced energy input compared with conventional solution-deposition processes. Because this mechanism is independent of solution chemistry and oxide formulation, the platform is broadly applicable to diverse solution chemistries, crystalline oxides, and substrates. As a representative demonstration, $BiFeO_3$ perovskite films are fabricated on flexible polyimide substrates, producing biocompatible, multifunctional flexible films.

1. Introduction

Metal oxide films are essential materials driving the advancement of modern smart electronics.[1,2] As the demand for high-performance components continues to grow, these technologies increasingly rely on materials with multifunctional capabilities. Consequently, there has been a rapid expansion in the development and application of electronic devices based on multifunctional metal oxide films. However, this growth has raised pressing environmental concerns, including high energy consumption, carbon emissions, and electronic waste.[3,4] In response, there is a growing emphasis on sustainable fabrication methods that minimize environmental impact. These include reducing processing temperatures and energy inputs, as well as using non-toxic, earth-abundant materials in accordance with the principles of green chemistry and the circular economy.[5,6]

One of the most critical factors influencing the performance of metal oxide layers is their degree of crystallinity, as many of their key optical, magnetic, and electrical properties are intrinsically linked to their crystal structure.[7–9] Therefore, enhancing the crystallization of metal oxide films is essential for improving their functional properties.

Simultaneously, modern smart electronics increasingly require the integration of these films with low-cost, thermally sensitive substrates (*e.g.*, plastics, paper). These substrates degrade at temperatures significantly lower than those typically used in conventional oxide processing. Therefore, this thermal mismatch necessitates the development of low-temperature fabrication methods that preserve substrate integrity while ensuring high-quality film formation.

Among the various deposition techniques, Chemical Solution Deposition (CSD) has emerged as a promising approach for fabricating oxide thin films. This is because CSD offers advantages in cost, scalability, and deposition rate, relying on soft chemistry routes primarily based on sol–gel synthesis.[1] These methods typically use alkoxide precursors, which, despite their high reactivity toward hydrolysis and

[a] Instituto de Ciencia de Materiales de Madrid (ICMM), CSIC, C/Sor Juana Inés de la Cruz, 3, 28049, Madrid, Spain. E-mail: lcalzada@icmm.csic.es
[b] Centro de Astrobiología, CSIC-INTA, Campus ESAC, Camino bajo del castillo s/n, E-28692 Villanueva de la Cañada, Madrid, Spain
[c] Dpt. Física de la Tierra y Astrofísica, Facultad de Ciencias Físicas, Universidad Complutense de Madrid (UCM), E-28040 Madrid, Spain
[d] Facultad de Ciencias, Universidad Autónoma de Madrid (UAM), Ciudad Universitaria de Cantoblanco, E-28049 Madrid, Spain
[e] Instituto de Tecnología Química (UPV-CSIC), Universitat Politécnica de Valencia – Consejo Superior de Investigaciones Científicas, E-46022, Valencia, Spain

limited solution stability, can be chemically modified to tailor their physicochemical properties. The incorporation of functional alcohols, β-diketones, amines, and other chemical agents during solution synthesis can significantly influence parameters such as hydrolysis rate, solubility, and viscosity, while also enhancing colloidal stability. These modifications not only improve the quality of the deposited films but also enable their transformation into metal oxides at relatively low temperatures.[10–13]

A major challenge in CSD is controlling the hydrolysis and condensation reactions that are fundamental to solution-based film deposition. These reactions often occur simultaneously and rapidly, leading to uncontrolled gelation of the deposited layer. Premature gelation hinders the formation of a fully connected metal–oxygen (–M–O–M–) network, which is essential for promoting atomic ordering and the development of a crystalline phase under minimal thermal load. Therefore, a key objective in the CSD fabrication of high-performance metal oxide films is the precise adjustment of hydrolysis and condensation kinetics to enable the formation of the crystalline metal oxide films.[14] To address this issue, CSD strategies have been mostly driven toward the incorporation of hydroxyl (OH^-) groups into the chemical system using various OH^--donor compounds directly added into the precursor solution.[15–17]

In a different area of materials science, an innovative synthesis strategy was developed to accelerate the crystallization of aluminosilicate (zeolite) materials, in which highly reactive $^{\bullet}OH$ radicals were generated under UV irradiation in hydrothermally treated solutions to promote zeolite crystal nucleation, providing an alternative to conventional OH^--releasing compounds for catalyzing the polymerization of aluminosilicate anions around hydrated cations.[18]

In the field of metal oxide films, to the best of the authors' knowledge, $^{\bullet}OH$ radicals have been very rarely used and, when employed, generated exclusively in the precursor solution (liquid phase)[19] *via* photolysis of metal–ligand reagents to promote polycondensation, densification, and impurity removal in solution-derived dielectric and semiconductor films.

Building on this concept, our group first explored the use of hydroxyl radical ($^{\bullet}OH$) atmospheres for the solution deposition of metal oxide films on standard rigid silicon substrates employed in the semiconductor industry.[20] Unlike previous approaches, gaseous $^{\bullet}OH$ radicals are now generated directly within the processing atmosphere in a controlled manner *via* UV irradiation, enabling direct interactions with the evolving film surface. This interaction simplifies the complex, multistep decomposition processes characteristic of conventional solution-based deposition of metal oxide films and redirects the reaction pathway toward a simple, one-step decomposition mechanism. As a result, an amorphous oxide film is readily formed and can be converted into the crystalline phase with minimal energy input.

This one-step decomposition pathway for solution-derived oxide films is demonstrated to be a versatile and effective synthesis platform for solution-processed metal oxide thin films. In contrast to conventional thermal or solely UV-assisted deposition methods,[21,22] the present approach provides precise control over the entire reactive synthesis environment, enabling deliberate activation of film formation in the three distinct regions involved in solution-derived film processing: the surrounding atmosphere, the film–atmosphere interface, and the bulk of the film.

The reaction mechanisms governing this synthesis platform are elucidated using a suite of complementary physicochemical characterization techniques specifically designed to probe the evolving reaction system. Collectively, these analyses provide a comprehensive mechanistic understanding of film formation and support the broad applicability of this processing strategy across a wide range of metal oxide compositions, independent of the specific precursor chemistry employed in chemical solution deposition.

2. Results and discussion

A model chemical system was employed to demonstrate synthesis control and efficiency in this thin-film solution processing platform. Thus, the precursor solution consists of a combination of metal reagents, solvents and additives commonly used in the CSD fabrication of transition metal oxide thin films. These respectively include metal alkoxides and salts; alcohols, polyols, carboxylic acids and anhydrides; and coordinating ligands based on β-diketonates and amines (Fig. S1). As a representative multimetal oxide composition, the bismuth ferrite (Mn-doped $BiFeO_3$) perovskite was chosen.[23] This selection enables a deeper understanding of the underlying mechanisms that take place in this processing method.

In addition, a preliminary investigation was conducted to assess the influence of different processing atmospheres—namely, a conventional O_2 atmosphere commonly employed in solution-processed film fabrication,[14] and a rarely used $O_2 + H_2O$ vapor atmosphere[17]—with and without UV irradiation of freshly solution-deposited films (Fig. S2).

These studies enabled the rational design of the steps underlaying the $^{\bullet}OH$-atmosphere radical-assisted fabrication platform developed in this work (Fig. 1). The process comprises the following steps: solution deposition of the film onto the substrate (Step 1); treatment of the film in a $^{\bullet}OH$ radical atmosphere (Step 2); treatment of the film in an O_3 atmosphere (Step 3); and low-temperature thermal treatment to obtain the crystalline film (Step 4). Fig. S3 presents a detailed schematic illustrating the different steps of the process.

Fig. 2a provides direct evidence for the generation of free radicals at the Step 2 of this fabrication process. The Electron Paramagnetic Resonance (EPR) spectra of the spin-trapping agent 5,5-dimethyl-1-pyrroline *N*-oxide (DMPO), both before and after the exposure to a $^{\bullet}OH$-rich atmosphere, are shown in this figure. While the spectrum of the unexposed DMPO shows only background noise, the post-exposure spectrum reveals signals ascribed to two distinct radical species: one corresponding to the 5,5-dimethyl-1-pyrroline *N*-oxyl (DMPOX) adduct, and the other attributed to degradation products of the $^{\bullet}OH$-DMPO adduct.[24,25] The simultaneous appearance of these

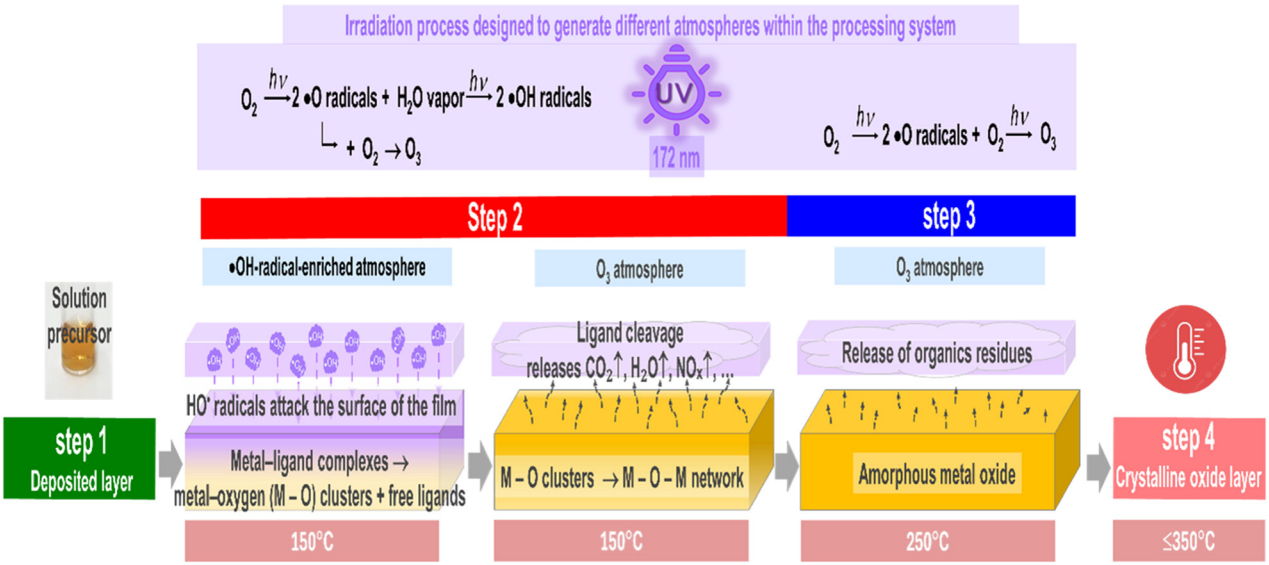

Fig. 1 Irradiation process developed for the hydroxyl free radical method, designed to accelerate the formation and crystallization of solution-processed functional metal oxide thin films, while operating under atmospheres generated within the processing system. The scheme illustrates the successive steps of the method: (Step 1) solution deposition of the film onto the substrate; (Step 2) treatment of the film in a •OH radical atmosphere; (Step 3) treatment of the film in an O_3 atmosphere; and (Step 4) low-temperature thermal treatment to obtain the crystalline film. The drawings representing the characteristics of the films obtained after the different steps of the devised process are shown at the bottom. See also Fig. S1 and S3.

two signals indicates a high concentration of •OH radicals in the processing atmosphere, exceeding the trapping capacity of DMPO.[25,26] This overproduction of hydroxyl radicals is attributed to the high energy of the UV irradiation source used in this process, an excimer lamp with λ = 172 nm. Thus, the high-energy UV exposure promotes secondary oxidation reactions of the DMPO that lead to the formation of DMPOX, as well as the decomposition of the •OH-DMPO adduct into a more stable paramagnetic dimer, which is responsible for the symmetrical 1 : 1 : 1 triplet observed in the spectrum.

Fig. 2b–f present a detailed analysis of the vibrational modes identified in the Infrared Reflection Absorption Spectroscopy (IRRAS) spectra of the solution-deposited $BiFeO_3$ thin films at the different steps of the processing method. The results obtained under the hydroxyl radical-rich atmosphere are compared with those obtained in counterpart films processed using conventional conditions (*i.e.*, without the generation of •OH radicals due to the lack of UV irradiation and water vapor). This comparison enables an accurate assessment of the stage at which functional groups are formed or eliminated during the process and how this influences the structural evolution of the film. As shown in Fig. 2b, the generation of •OH radicals results in a pronounced increase in O–H bond formation at Step 2 compared to the conventional system. These bonds are rapidly eliminated in Step 3, just after the photogenerated •OH radicals attack the film surface and initiate primary reactions with different hydrocarbon chains belonging to the metal complexes, as deduced from Fig. 2c. The cleavage of these bonds occurs at a high reaction rate, as indicated by the exponential decay of C–H bonds from Step 1 to Step 2. In contrast, in the conventional process, C–H bond cleavage occurs more gradually at Step 2 and it is only completed after Step 3. It should be noted that, according to Fig. 2d, the cleavage of C–O bonds follows a similar trend to that of C–H bonds. On the contrary, the cleavage mechanisms of C–C and C═O bonds, as inferred from Fig. 2e, do not differ significantly between the conventional process and the •OH radical-assisted method. These functional groups appear to be among the last to be cleaved from the system. From this and in comparison with previous results, the cleavage of these bonds seems to proceed slower in the initial stages of the conventional process. Finally, the band assigned to C═N bonds in Fig. 2f is attributed to the methyldiethanolamine ligand coordinated to bismuth in the Bi-*mdea* complex. Upon coordination, a partial double bond character develops between the nitrogen atom and the adjacent carbon,[27,28] which is reflected in the IR spectrum as a band in the 1600–1650 cm^{-1} region. This signal resembles that of an imine bond (C═N), although it does not correspond to a true imine group.[28] Note that this band reaches a maximum intensity at Step 2 across both processing methods. However, under a •OH-rich atmosphere, the presence of these groups is significantly reduced with only trace amounts detected. This result indicates that the Bi-*mdea* complex is rapidly decomposed in the presence of •OH radicals at Step 2.

The decomposition of metal precursors and intermediate compounds is further supported by the appearance of the CO_2 band between 2300–2400 cm^{-1} in the IRRAS spectra. Fig. 3a and b respectively illustrate how the integrated area of the CO_2 IRRAS mode and that of the broad signal recorded below 750 cm^{-1} – mainly resulting from ν(M–O) stretching vibrations – evolve throughout the different steps of the fabrication processes. The early removal of organic components under the •OH radical atmosphere leads to the observation of CO_2 elimination only at Step 2, which is accompanied by a

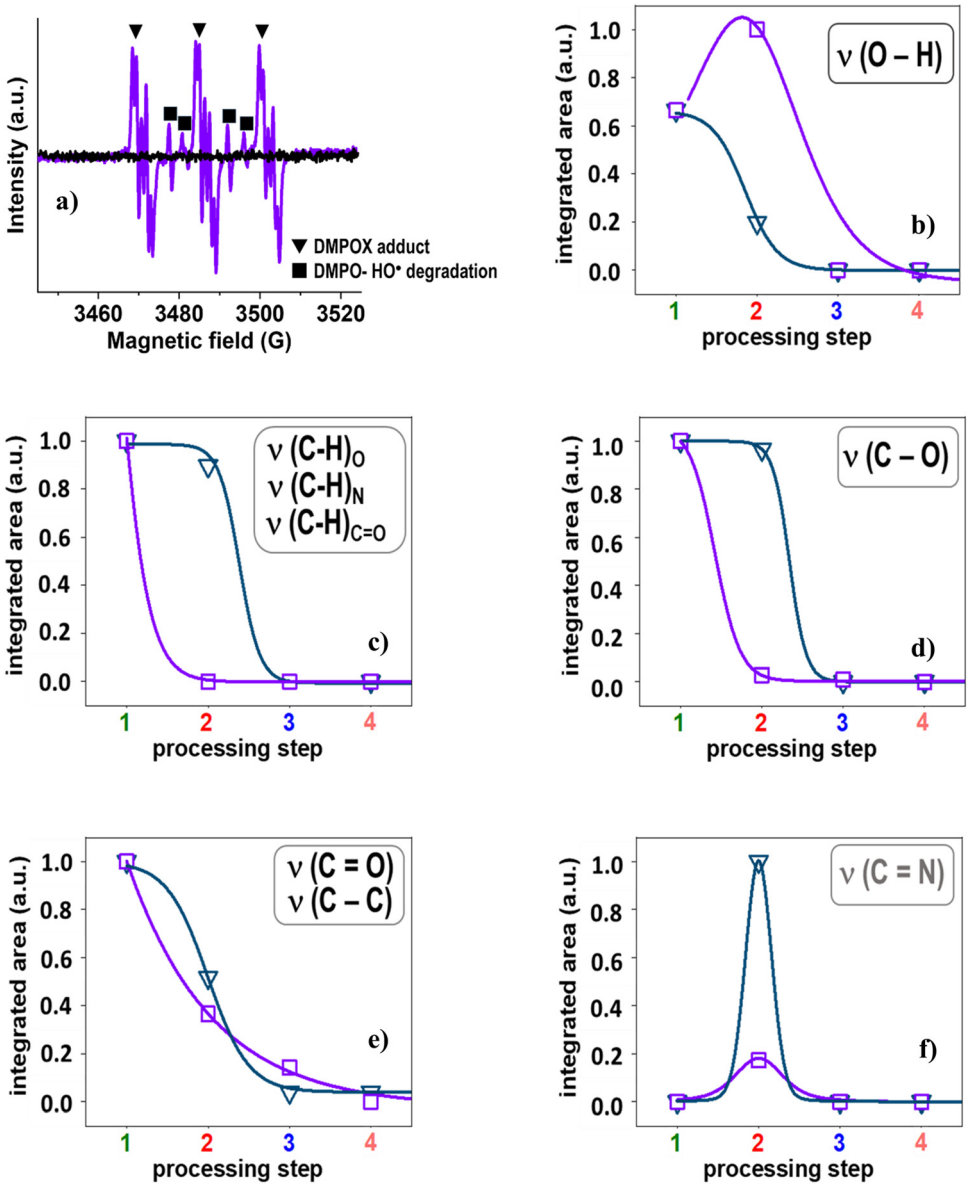

Fig. 2 (a) Detection of hydroxyl radicals (•OH) generated under UV irradiation in the surrounding atmosphere during Step 2 of the processing method. This was achieved by comparing the Electron Paramagnetic Resonance (EPR) spectrum of the DMPO spin-trapping agent after exposure (violet line) with that of an untreated DMPO sample (black line). EPR signal assignments: ▼ indicate the DMPOX adduct, and ■ correspond to the degradation products of the •OH-DMPO adduct. (b)–(f) Integrated areas of selected vibrational modes obtained from IRRAS analysis of the film at various stages of the solution deposition process assisted by an •OH-rich atmosphere. These are compared to the corresponding values from the conventional solution deposition method performed in air. The integrated areas of the ν(O–H) and ν(C═N) bands were normalized to the maximum values observed at Step 2 of the •OH-radical-assisted and conventional processes, respectively. In the former, new O–H bonds form during this step. A comprehensive analysis is presented in Fig. S4a, which includes results obtained under •OH radical, air, and H_2O vapor atmospheres. Fig. S5 further illustrates the generation of a •OH-radical-enriched processing atmosphere.

pronounced decrease in the integrated area of the IRRAS signal below 750 cm^{-1} from Step 1 to Step 2. In the conventional process, this transformation occurs much more gradually, with only slight changes in the integrated area of the signal below 750 cm^{-1}, while continuous CO_2 elimination is recorded up to Step 4 during prolonged annealing at 350 °C.

Fig. 3c and d present the IRRAS spectra of the signal recorded below 750 cm^{-1}, primarily attributed to the ν(M–O) band.[29] In both the •OH radical-assisted and conventional processes, the broadness of this IRRAS signal in solution-deposited gel layers originates from the presence of multiple types of M–O bonds in distinct chemical environments, associated with groups such as M–OR and M–OH, where M represents bismuth, iron, or both. To evaluate the possible contribution of M–N bonds to this broad band, the figures also include the corresponding FTIR spectra in the region extending from below 750 cm^{-1} down to beyond 200 cm^{-1}, where M–N stretching modes are typically observed. However, due to

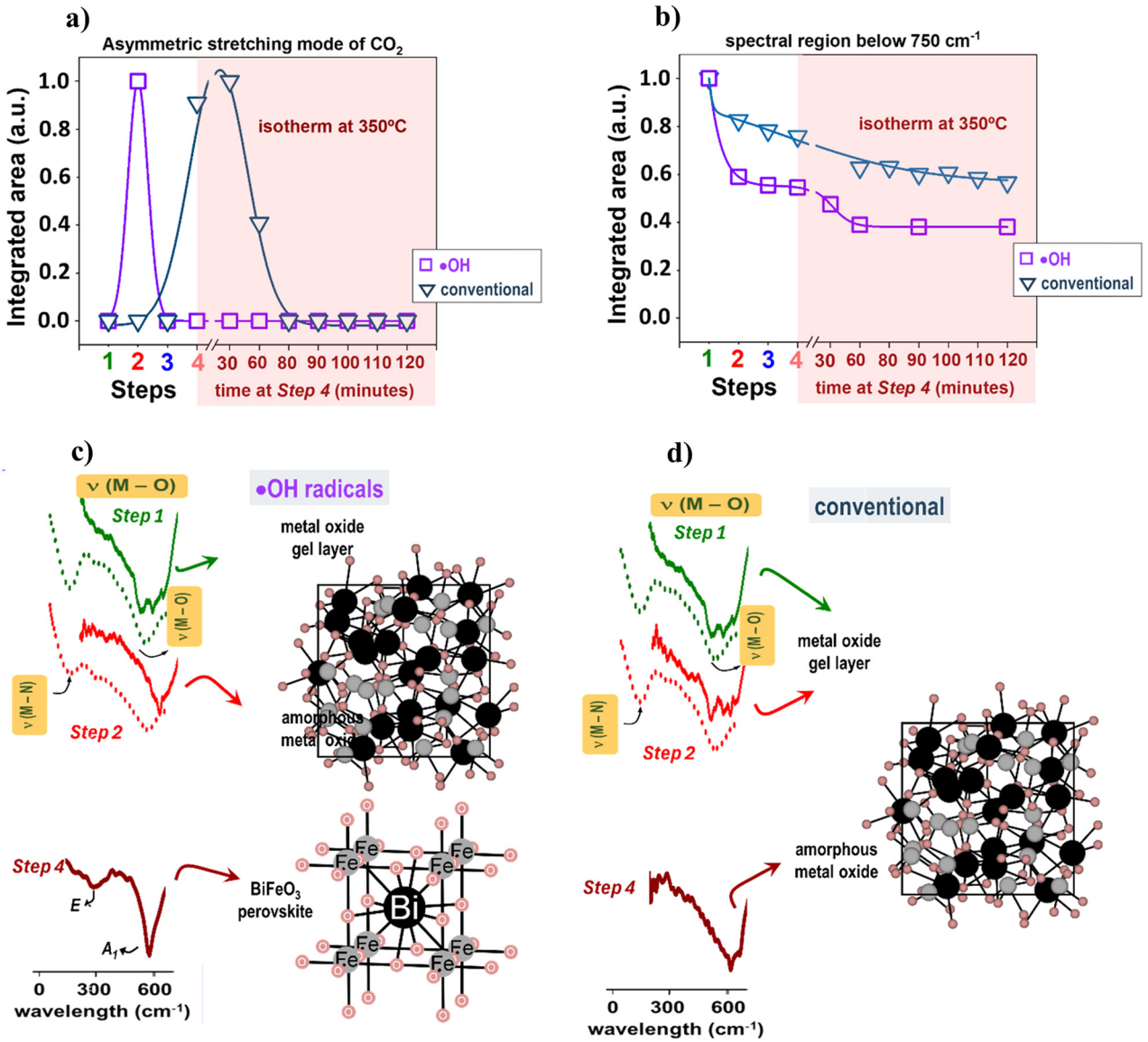

Fig. 3 (a) and (b) Integrated areas calculated from the IRRAS spectra of the films at each stage of the •OH-assisted deposition process and the conventional process in air, corresponding to: (a) the asymmetric stretching vibration of CO_2 observed around 2349 cm^{-1}, and (b) the broad absorption band detected below 750 cm^{-1}. The integrated area of the CO_2 vibrational mode was normalized to the maximum values observed at Step 2 of the •OH-radical-assisted process and at Step 4 (with a soaking time of 30 minutes) of the conventional process. A comparative analysis of the signal evolution under different processing atmospheres is provided in Fig. S4b. (c) and (d) FTIR analysis (represented by the dashed green and red curves) in the spectral region below 750 cm^{-1}, mainly associated with metal–oxygen and metal–nitrogen vibrations. Measurements were performed on pellets prepared by mixing the bismuth gel precursor samples – obtained after Steps 1 and 2 – with polyethylene ($(C_2H_4)_n$), which is transparent in this spectral range. The data correspond to both the •OH-assisted process (c) and the conventional process in air (d). Solid lines represent the IRRAS spectra recorded from the films at Steps 1, 2, and 4, the latter after thermal treatment at 350 °C for 60 min. These are shown as green, red, and brown solid lines, respectively. The drawings shown next to the spectra in (c) and (d) provide an approximate representation of the structural characteristics of the films obtained at Steps 2 and 4.

substrate interference in this low-frequency range, direct measurements on deposited layers were not feasible. Instead, the analysis was conducted using pellets prepared by mixing precursor gel samples with polyethylene, a material transparent in this spectral region. Each spectrum is accompanied by a schematic illustration providing an approximation of the structural characteristics of the films at Steps 2 and 4.

Fig. 3c reveals an abrupt narrowing of the IRRAS signal from Step 1 to Step 2 in samples processed under the •OH radical atmosphere. This change is accompanied by a significant reduction in the FTIR ν(M–N) band, specifically due to the rupture of Bi–N bonds in the Bi-*mdea* complex. Concurrently, Step 2 marks the near-complete removal of organic species, as evidenced by the evolution of the CO_2 mode shown in Fig. 3a. These transformations facilitate the crosslinking of M–O bonds into extended M–O–M chains. As a result, from Step 2 onward, the IRRAS signal in this spectral range remains relatively stable through Steps 3 and 4 (Fig. 3b), ultimately leading to the

splitting of the band into two distinct modes observed in Fig. 3c at Step 4, as annealing time at 350 °C increases. These modes correspond to the rhombohedral $BiFeO_3$ perovskite structure,[30] confirming the formation of a crystalline $BiFeO_3$ thin film.

In contrast, Fig. 3d shows that at Step 2, the IRRAS and FTIR signals of the films obtained *via* the conventional process remain nearly unchanged from those recorded at Step 1. This indicates the absence of M–N bond rupture, limited organic matter removal (as supported by the lack of CO_2 release observed in Fig. 3a), and consequently, hindered crosslinking of M–O bonds (Fig. 3b). Only at Step 4, after prolonged annealing at 350 °C, does a narrower IRRAS feature emerge, comparable to that observed at Step 2 in the •OH radical-assisted process (Fig. 3c). However, the characteristic IR spectrum of the $BiFeO_3$ perovskite[30] is never observed. This suggests that the structural state reached at Step 4 in the conventional process corresponds to an amorphous metal–oxygen network, similar to the one formed much earlier at Step 2 under •OH radical exposure. This amorphous state appears to be ''frozen,'' as further annealing at 350 °C is insufficient to reorganize the M–O bonds into an ordered crystalline structure.

To gain more insight into the decomposition pathway of the metal precursors assisted by this hydroxyl radical-assisted method, Electrospray Ionization Mass Spectrometry (ESI-MS) and Atmospheric Pressure Chemical Ionization Mass Spectrometry (APCI-MS) were employed. Samples were collected from gel precursors obtained at Step 2 of the process, both with and without exposure to a •OH atmosphere. The corresponding spectra are shown in Fig. 4a–d, together with the molecular structures of the respective Bi-*mdea*[31–33] and Fe-*acac*[34] complexes. This analysis demonstrates that the attack of the gaseous •OH radicals to the system leads to the dissociation of the metal complexes during the early stages of the process (Step 2). Specifically, cleavage of Bi–N and Bi–O bonds in the Bi-*mdea* complex, as well as Fe–O bonds in the Fe-*acac* complex, occurs. As a result, only fragments corresponding to the free *mdea* and *acac* ligands are ionized, as shown in Fig. 4a and b.[35] While ESI-MS analysis of the Bi-*mdea* precursor revealed a dominant fragment with 100% intensity at *m/z* 120.10, corresponding to the free *mdea* ligand ($C_5H_{14}NO_2$) (Fig. 4a), the Fe-*acac* precursor exhibited poor ionization efficiency under ESI-MS. As a result, APCI-MS was used instead for the iron precursor. In this case, the spectrum revealed fragments associated with various *acac* adducts (Fig. 4b). Specifically, the APCI-MS data indicated the presence of adducts composed of three and four *acac* units, along with a larger cluster containing six to seven units. These signals are likely attributable to the typical formation of gas-phase clusters during ionization, as well as to modified clusters that may have undergone partial dehydration and interacted with the solvent used in the analysis, dichloromethane (CH_2Cl_2). The absence of Bi or Fe in the structure of the fragments detected here suggests that the metal cations have already been incorporated into a metal–oxygen network formed as early as Step 2. In contrast, when the Bi-*mdea* and Fe-*acac* precursors are conventionally processed in air, larger fragments are detected, indicating that both Bi and Fe remain coordinated to their respective ligands (*mdea* and *acac*), and no significant cleavage of the metal–ligand complexes occurs (Fig. 4c and d).

These findings strongly support the results presented in Fig. 2 and 3, providing further evidence for the key role of •OH radicals in promoting complete metal–ligand dissociation. Based on these experimental observations, the reaction pathway depicted in Fig. 5 is proposed to operate within the •OH-radical-atmosphere-assisted fabrication platform developed in this work for oxide thin films, and is specifically described here for multifunctional $BiFeO_3$ perovskite layers. During Step 2, •OH radicals generated in the processing atmosphere interact with the film surface and induce a one-step decomposition pathway throughout the bulk of the film. This process is characterized by the attack of •OH radicals on metal–ligand bonds, leading to their cleavage, specifically Bi–N and Bi–O bonds in the Bi-*mdea* complex and Fe–O bonds in the Fe-*acac* complex. This process results in complete ligand detachment and the formation of highly reactive •OH–metal nanoclusters.

The free ligand fragments are efficiently and rapidly removed from the film *via* oxidation, as evidenced by CO_2 evolution occurring exclusively during Step 2. Within the film, the reactive •OH–metal clusters undergo cross-linking and reorganize into an amorphous M–O–M network during Step 3. This network serves as a robust scaffold for the guided formation of the crystalline phase, which can develop with minimal energy input (top of Fig. 5). In contrast to the one-step decomposition pathway occurring within the film under the •OH-radical-atmosphere-assisted deposition platform, the conventional solution deposition process follows a distinctly different pathway, in which precursor thermal degradation occurs *via* a multi-step mechanism that generates multiple intermediates, delaying the onset of perovskite crystallization (bottom of Fig. 5).

By employing this thin-film solution-processing platform for oxide films, based on the use of •OH-radical-assisted atmospheres in a fabrication process that enables precise control over the entire chemical reaction system during film formation, functional $BiFeO_3$ perovskite thin films have been synthesized at significantly lower temperatures ($\leq$350 °C) than those conventionally required for this class of materials. Despite the low processing temperature, these films exhibit performance comparable to that of films fabricated at high temperatures. To demonstrate this, $BiFeO_3$ films were deposited on Pt-coated (100)Si substrates, those commonly used in microelectronics, and processed under a low thermal budget of 350 °C for 60 minutes. The results presented in Fig. S6 and S7 confirm that the films display enhanced multifunctional properties, such as ferroelectricity and ferromagnetism, which are extremely valuable for integration into high-performance, metal oxide-based smart devices. Accordingly, their performance favorably compares with that of most low-temperature, solution-processable functional oxides (including ferroelectric, multiferroic, and semiconducting materials), particularly organic counterparts.[36–38] These results are transferable to other complex ferroelectric compositions, such as the quaternary oxide $PbZr_{0.3}Ti_{0.7}O_3$ (PZT) – the most widely adopted

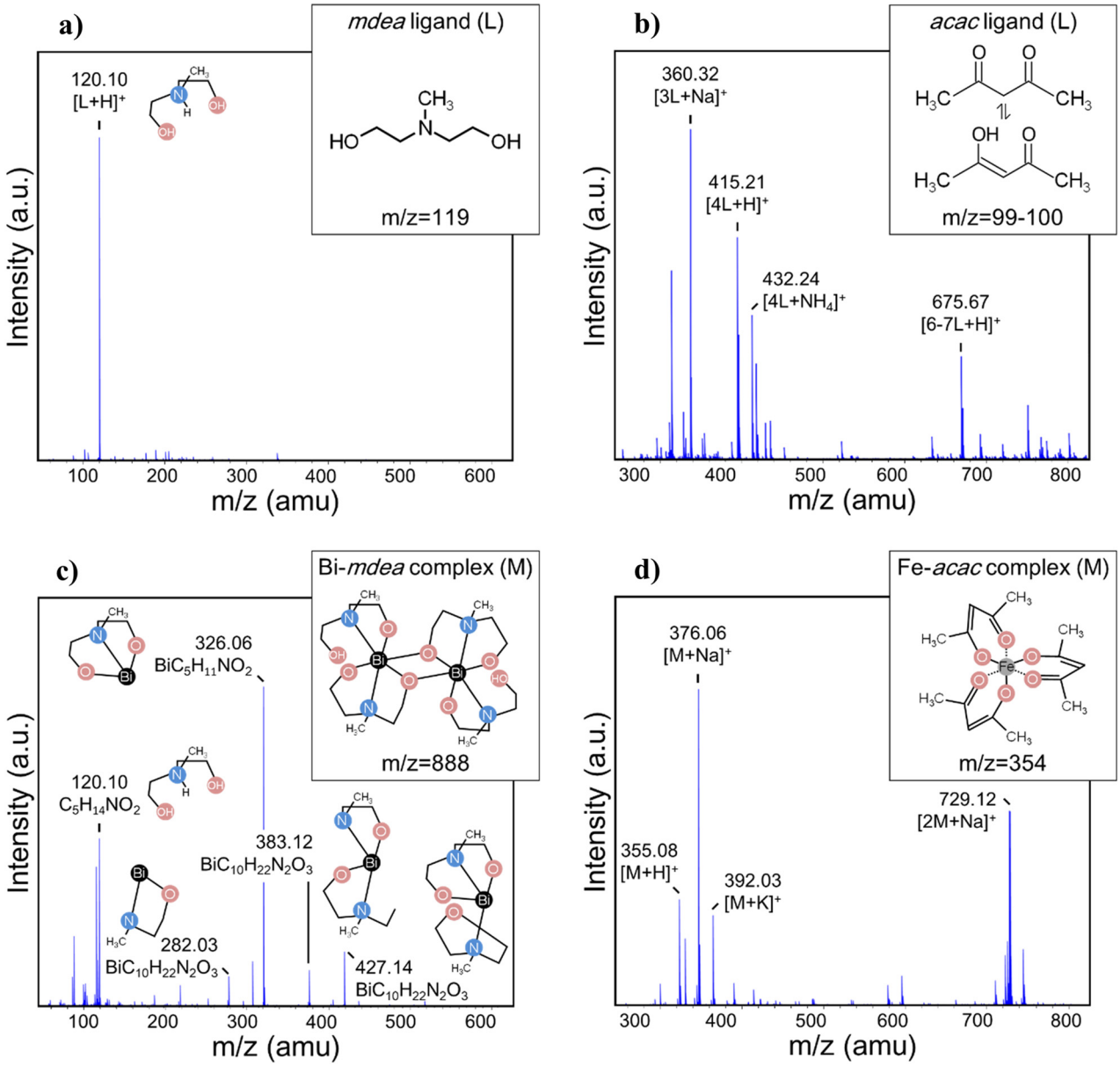

Fig. 4 (a) and (b) Electrospray Ionization Mass Spectrometry (ESI-MS) and Atmospheric Pressure Chemical Ionization Mass Spectrometry (APCI-MS) spectra of the Bi-*mdea* and Fe-*acac* precursors, respectively, obtained at Step 2 under an atmosphere enriched with gaseous hydroxyl (•OH) radicals. In the spectrum shown in (b), the signals correspond to adducts of the *acac* ligand (nL), formed mainly through the aggregation of protonated neutral species.[35] (c) and (d) Corresponding spectra of the Bi-*mdea* and Fe-*acac* precursors processed using the conventional method in air.

ferroelectric oxide in commercial applications. Using this processing platform, PZT ferroelectric films were prepared with a low thermal load, yielding crystalline perovskite-phase films with performance comparable to that of films fabricated at higher temperatures (Fig. S8).

Of particular significance is the fact that the reduced thermal load achieved allows for the crystallization of oxide layers at temperatures compatible with low-cost, thermosensitive substrates such as flexible polyimide (PI). Furthermore, the solution-based nature of the fabrication process facilitates large-area deposition, a critical requirement for emerging flexible electronics. Fig. 6a shows the successful growth of $BiFeO_3$ thin films directly on PI, revealing surface and cross-sectional microstructures composed of nanosized grains. Although the XRD pattern of this sample displays broad reflections ascribed to the polymer substrate, distinct peaks corresponding to the $BiFeO_3$ perovskite phase are clearly observed.

A photograph of the flexible sample, along with its ferroelectric and ferromagnetic responses, are shown in Fig. 6b–d. The flexible films exhibit a remanent polarization (P_R) of approximately 10.0 μC cm^{-2} and a saturation magnetization (M_S) of around 1.1 emu cm^{-3} at room temperature. Both P_R and M_S values are reduced compared to those obtained in equivalent films deposited on rigid Si substrates ($P_R \sim 29.0$ μC cm^{-2}

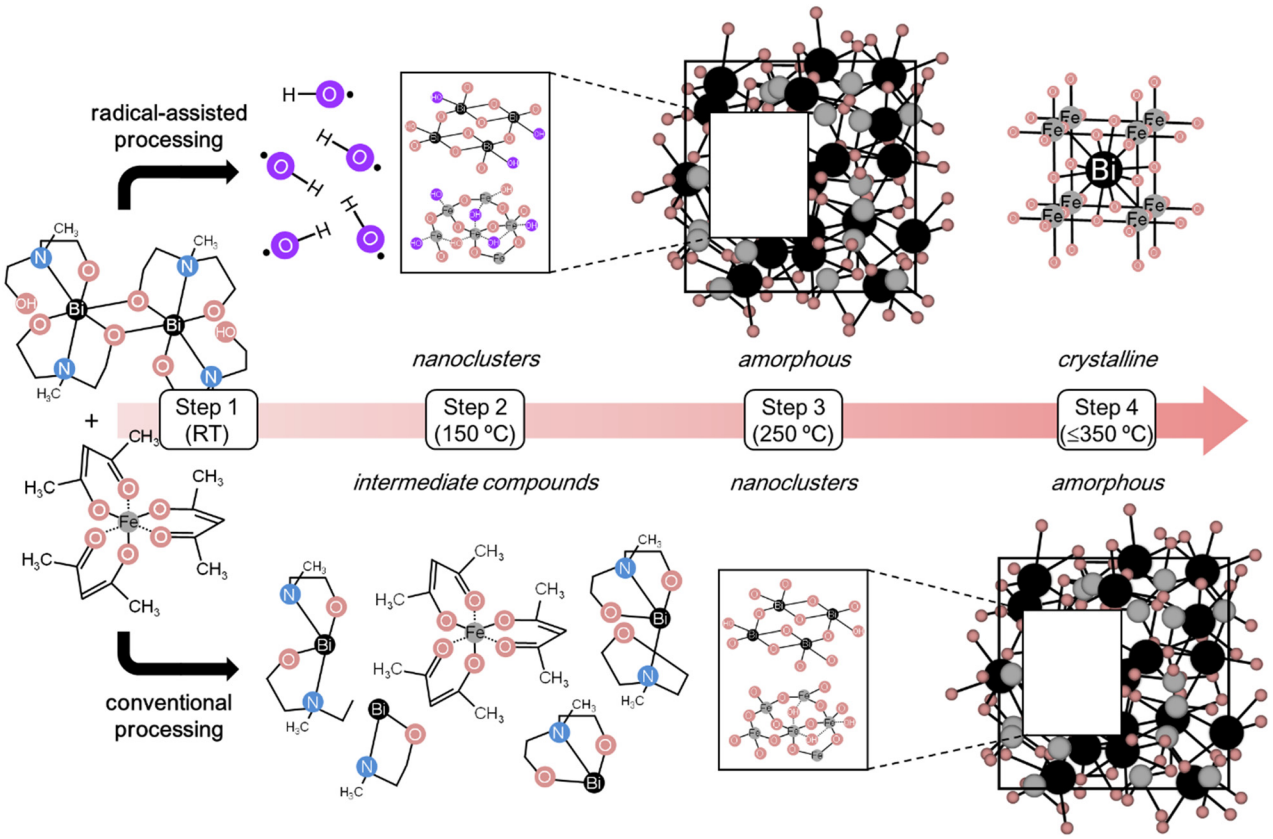

Fig. 5 The top of the figure illustrates the proposed decomposition mechanisms of the Bi-*mdea* and Fe-*acac* metal complexes under UV-induced generation of hydroxyl radicals (•OH) in the processing atmosphere. The violet color highlights the *in situ* generated •OH radicals, the •OH groups coordinated to the metal (•OH–metal clusters), and the oxygen (O) atoms bonded to the metal (metal–oxygen network), all of which participate in the proposed reaction pathway. The bottom of the figure illustrates the decomposition mechanisms of the Bi-*mdea* and Fe-*acac* metal complexes under conventional processing in an air atmosphere.

and $M_S \sim 3.0$ emu cm^{-3}), indicating a smaller fraction of the multiferroic $BiFeO_3$ phase in the flexible film on PI compared with the rigid film on Si (see Fig. S7).

In contrast, the latter film on Si shows a M_S value comparable to that of the $BiFeO_3$ film conventionally processed at 500 °C on Si (3.1 emu cm^{-3}), suggesting that the total volume of the ferromagnetic phase is in a rough approximation, essentially the same in both the low- and high-temperature processed films. However, the P_R value of ~29.0 μC cm^{-2} is markedly lower than the 46.0 μC cm^{-2} measured in the conventionally processed $BiFeO_3$ film at 500 °C on Si. This functional response indicates that, although the overall volume of the $BiFeO_3$ multiferroic phase is similar in both films, in the low-temperature processed film this phase is not fully available for switching. Considering that ferroelectricity is a cooperative phenomenon requiring continuity between the capacitor electrodes, regions of the ferroelectric phase that are not electrically connected within the device cannot switch under the applied electric field. This leads to a reduced functional ferroelectric response and, consequently, a lower P_R value.

The distinct cross-sectional microstructures observed in Fig. S6 and S7 – columnar grain growth for the high-temperature film on Si and polycrystalline grain growth for the low-temperature film on Si – may explain this behavior. It is likely that the intergranular porosity present in the low-temperature processed film, oriented perpendicular to the applied electric field, disrupts ferroelectric switching during poling. This interruption prevents efficient poling due to the lack of continuous ferroelectric pathways. As a result, because ferroelectricity is inherently cooperative, not all regions of the ferroelectric phase can respond to the applied field, leading to the lower P_R value observed in the low-temperature processed film compared to the high-temperature processed one.

Consequently, these results clearly demonstrate that the characteristics of multiferroic $BiFeO_3$ perovskite films differ significantly depending on whether they are processed at high or low temperatures. Moreover, by comparing the functional response of films deposited on rigid Si and flexible PI substrates, it becomes evident that their functionality also varies markedly, being notably reduced in the flexible $BiFeO_3$ film. These differences are likely related not only to the distinct mechanical constraints imposed by the two types of substrates but also to variations in the nature of the film–substrate interface that develop in each case. Such differences appear to influence the nucleation of the ferroelectric oxide phase, leading to a higher fraction of the multiferroic $BiFeO_3$ perovskite

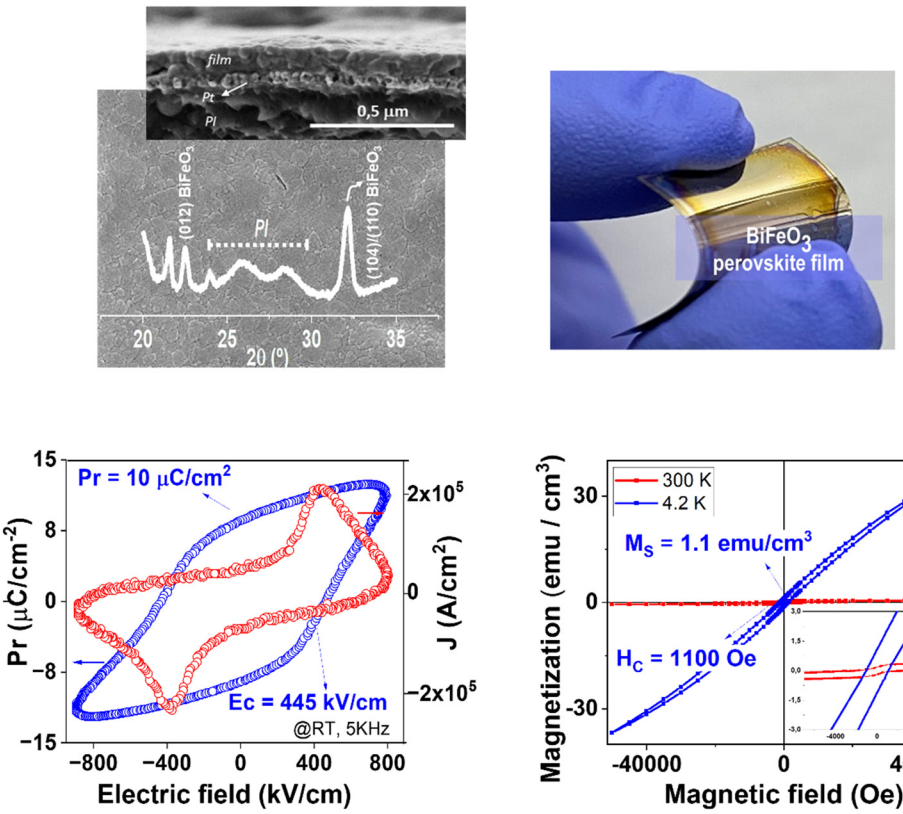

Fig. 6 (a) SEM surface and cross-sectional images of these $BiFeO_3$ films directly deposited on flexible polyimide (PI) substrates. The corresponding XRD pattern of these films on PI is also included. (b) Photograph of the flexible $BiFeO_3$ film on PI. (c) Ferroelectric hysteresis loop (P–E) and current density curve measured at @RT in the flexible $BiFeO_3$ film on PI. (d) Magnetization *vs.* Magnetic field (M – H) loops, measured at room temperature (@RT, 300 K) and low temperature (4.2 K), of the flexible $BiFeO_3$ film on PI.

phase in the films grown on rigid Pt-coated Si substrates. This behavior, combined with the widely reported reduction in ferroelectric performance at the nanoscale in low-temperature – processed samples, may have a pronounced impact on the functional properties of the flexible films.[39–41] Although this topic lies beyond the scope of the present study, it represents an important area for future research to address the specific requirements of flexible electronic devices.

The ferroelectric and ferromagnetic properties of these flexible $BiFeO_3$ thin films on PI highlight their strong potential for next-generation flexible electronic systems. On the other hand, the ferroelectric $BiFeO_3$ perovskite is a lead-free compound of great interest as a potential substitute for traditional lead-based ferroelectrics in electronic devices. This is particularly relevant in the context of European regulations, which require the elimination of lead from such systems. The significance of $BiFeO_3$ is especially notable in the development of multifunctional electronic devices. Furthermore, the appeal of $BiFeO_3$-based perovskite films would increase substantially if their biocompatibility were demonstrated, as this would pave the way for their use in bio-integrated devices. Accordingly, biocompatibility studies were conducted *in vitro* to explore the potential application of these $BiFeO_3$-based flexible electronic devices in environments compatible with living organisms and the biosphere as a whole, such as biomedicine and bio-integrated smart systems. The impact of integrating flexible $BiFeO_3$ films on PI substrates, and their relevance for future bio-integrative applications, was investigated *in vitro* with murine L929 fibroblasts (Fig. 7a–c). First, scanning electron microscopy studies revealed that cell cultures extensively colonized the entire surface of all components of the flexible device – including Pristine PI, NiCr-coated PI, Pt/NiCr-metallized PI, and the flexible $BiFeO_3$ film capacitor device (Fig. 7a(i–viii)). Importantly, cells maintained the typical spindle shape of fibroblasts, with the frequent observation of cells undergoing mitosis, thus proving the occurrence of cell proliferation on the substrates. Last but not least, L929 cells were also observed close in contact with the material at the periphery, again without showing evident morphological alterations or impairment of cell adhesion and proliferation in the near proximity of the different components of the device (Fig. 7a(ix–xii)).

In agreement with the electron microscopy results, the cultures extensively colonized the entire array surface, showing a predominance of live cells under all tested conditions, similar to what was observed on the control glass substrate (Fig. 7b(i–v)). Quantitative analysis confirmed comparable cell viability across all surfaces, as determined by the respective areas occupied by live and dead cells (Fig. 7c). In this bar graph, the proportion of dead cells is almost negligible, as clearly illustrated in the insets, which compare the statistically derived bar charts of the areas

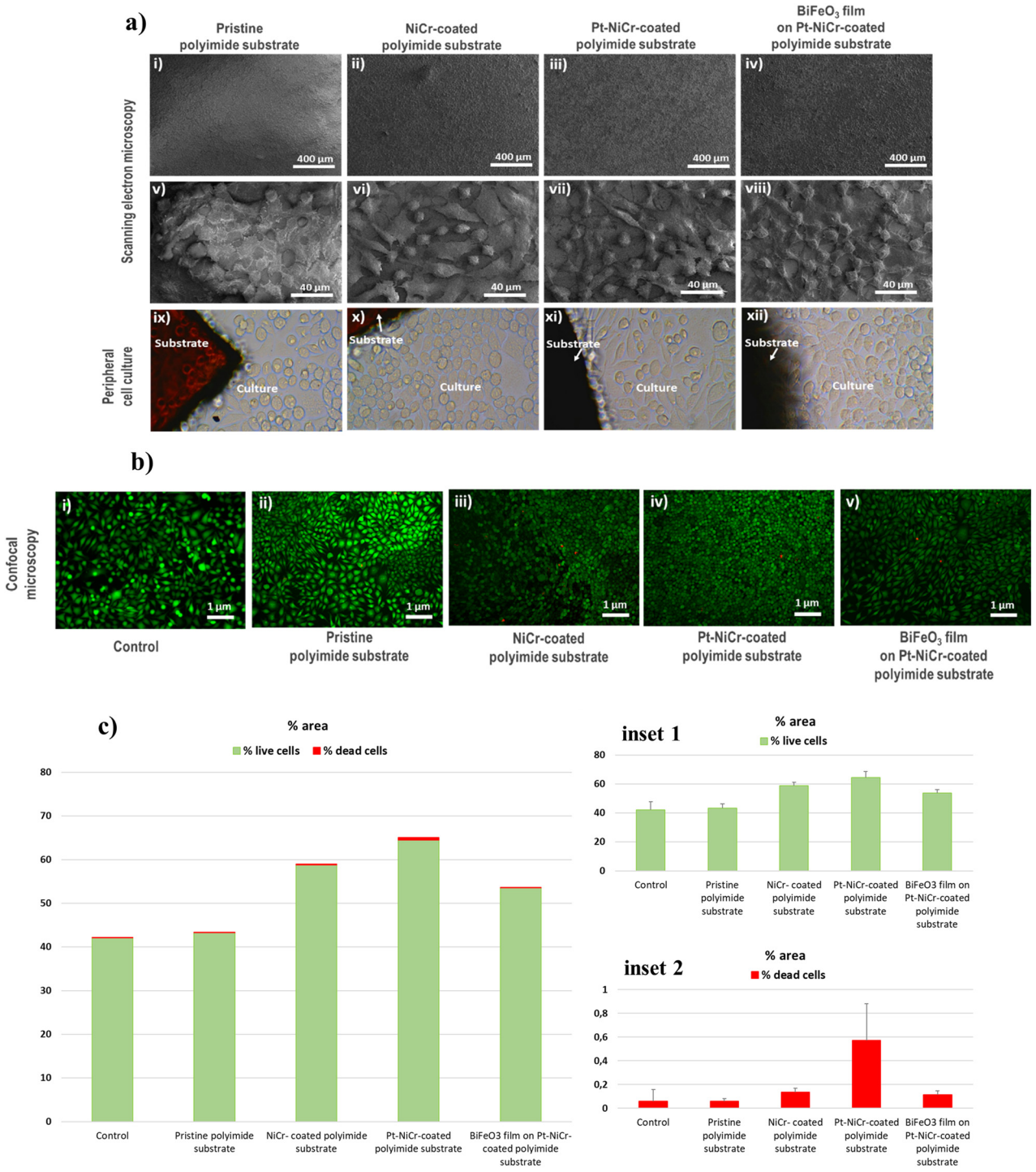

Fig. 7 (a) *In vitro* biocompatibility assessment of flexible $BiFeO_3$ thin films and their different components with murine L929 fibroblasts. (i)–(viii) Representative scanning electron microscopy (SEM) images of the cell cultures at two different magnifications. (ix)–(xii) Inverted optical microscopy images of the cell cultures at the periphery of the substrates. (b) Representative fluorescence images obtained by confocal laser scanning microscopy. (i)–(iv) correspond to the cell cultures colonizing the surface of all components of the flexible device and (v) correspond to the cell culture on the control glass substrate. Green (calcein) fluorescence corresponds to live cells and red (EthD-1) fluorescence to dead cells. (c) Quantitative viability results expressed as the area of positive staining and the corresponding percentages of area for live and dead cells. The insets illustrate the statistically derived bar charts of the areas occupied by live and dead cells. Note the different *y*-axis scales in both insets that highlight the minimum area covered by dead cells. Statistics: one-way ANOVA, with a significance of $p = 0.097$ (>0.05) for the live cells (inset 1) and of $p = 0.078$ (>0.05) for the dead cells (inset 2).

occupied by live and dead cells. The different *y*-axis scales in both diagrams highlight that the area covered by dead cells is minimal.

All together, these results demonstrate a high biocompatibility of these flexible ferroelectric films, and their components tested separately, with mammalian fibroblasts.[42]

We demonstrate the general applicability of this improved thin-film solution-processing platform, surpassing previous methods. The platform is specifically designed to enable rigorous control of the chemical reaction system during fabrication and is fully scalable using a single, simple UV irradiation source. Using this approach, high-quality films have been successfully fabricated across a wide range of metal oxide compositions, from binary oxides (TiO_2, Bi_2O_3) to quaternary oxides ($PbZr_{0.3}Ti_{0.7}O_3$), employing different metal precursors and solution chemistries (Fig. S7–S9).

Kinetic analysis carried out on single TiO_2 oxide films revealed that the activation energy (E_a) for crystallization in the low-temperature regime (≤ 350 °C) for the films processed with hydroxyl radicals is significantly lower than that calculeated for those metal oxide films obtained under conventional conditions (see Fig. S9). As a result, the onset of crystallization in single-oxide films occurs at an exceptionally low thermal budget, 250 °C for 30 minutes. This finding is particularly significant, as it underscores the versatility of this processing method for a wide variety of oxide layers, irrespective of the specific solution chemistry or metal precursor used (*e.g.*, metal–organic, metal–alkoxide, or metal–salt reagents). Therefore, the method demonstrates robust and general applicability across diverse solution formulations, enabling the low-temperature fabrication of high-quality oxide films from multiple precursor types.

We strongly believe that this methodology will unlock new chemical pathways for the advanced decomposition of metal oxide precursors and the low-temperature formation of thin-film materials. This approach enables the natural and efficient conversion of films into crystalline metal oxides with minimal thermal energy input. As such, it is particularly well-suited for direct integration onto low-cost, thermally unstable substrates, which are increasingly in demand in consumer smart electronics.

3. Conclusion

Highly reactive gaseous hydroxyl radical (•OH) atmospheres are employed to drive a one-step decomposition pathway in solution-derived oxide films. This approach stands in sharp contrast to conventional film–solution deposition processes, in which hydrolysis and condensation are catalyzed by hydroxide anions (OH^-) and proceed through multiple decomposition steps. The mechanism governing this synthesis procedure was elucidated using advanced physicochemical analytical techniques specifically adapted to study this solution-derived film reaction environment. These analyses revealed the formation of highly reactive hydroxyl radicals (•OH) within the surrounding film-processing atmosphere through their deliberate *in situ* UV-induced generation, which act as the driving force for the formation of the amorphous oxide film. Thus, these gaseous •OH radicals attack the film surface, inducing a one-step decomposition pathway within the solution-deposited layer. This process produces an organic-residue-free film composed exclusively of highly reactive •OH–metal clusters, which readily transform into an amorphous oxide film that can be easily converted into a crystalline oxide film under minimal thermal loads, requiring substantially reduced energy input, more than 30 °C lower than that of conventional solution-deposition processes.

This film solution synthesis strategy demonstrates versatility, robustness, and broad applicability, regardless of the solution chemistry or oxide formulation. Its application to various oxide films further highlights the scalable integration of crystalline oxide films onto low-cost, thermally sensitive substrates. This represents a groundbreaking advancement in the fabrication of high-performance crystalline oxide films for applications such as multifunctional, biocompatible flexible materials composed of complex metal oxide layers on polyimide.

4. Experimental section

Model precursor solutions containing the most common chemicals (*e.g.*, solvents, metal reagents, organic and ligand compounds) typically used in the sol–gel chemistry of transition metal oxides were prepared in this work. The novel solution deposition method developed here was tested on a ferroelectric perovskite oxide (the bismuth ferrite ($BiFeO_3$) perovskite). The synthesis of the $BiFeO_3$ precursor solutions was carried out using the reagents, molar ratios, and procedures described in detail at the top of Fig. S1. Two different solutions were synthesized for the bismuth and iron precursors. In the case of bismuth, a metal complex was synthesized by reacting Bi(III) with *N*-methyldiethanolamine ($CH_3N(CH_2CH_2OH)_2$, Aldrich, 99%; hereinafter *mdea*) in 1,3-propanediol solvent ($HO(CH_2)_3OH$, Aldrich, 98%; hereinafter *diol*) to obtain a solution of the Bi-*mdea* complex. For the preparation of the iron solution, commercial iron(III) trisacetylacetonate ($Fe(C_5H_7O_2)_3$, Aldrich $\geq$99.9%; hereinafter Fe-*acac*) was dissolved and refluxed in a mixture of diol and glacial acetic acid (CH_3CO_2H, Aldrich $\geq$99.7%). A third solution containing Mn(III) was obtained by reacting manganese(II) acetate tetrahydrate ($(CH_3COO)_2Mn{\cdot}4H_2O$, Aldrich $\geq$99%) in propionic acid (CH_3CH_2COOH, Aldrich $\geq$99.5%) to eliminate the crystallization water, followed by dissolving in diol under reflux conditions. This manganese-containing solution was used to fabricate Mn-doped $BiFeO_3$ films. For all the cations, the synthesized solutions were dissolved in dried ethanol (CH_3CH_2OH, Aldrich, dried, max. 0.01% H_2O) to achieve a 0.25 mol L^{-1} equivalent concentration (equivalent moles of the oxide). The solutions were then mixed in appropriate amounts to obtain a precursor solution of $Bi_{1.05}Fe_{0.95}Mn_{0.05}O_3$ (hereinafter $BiFeO_3$) with an equivalent concentration of 0.1 mol L^{-1}. This composition corresponds to the $BiFeO_3$ perovskite with a 5 mol%

excess of Bi(III) to compensate for possible bismuth volatilization and increase atoms diffusion by creating a fluid phase during processing. A 5 mol% Mn(III) doping was incorporated to the perovskite composition to increase resistivity and reduce losses in the final film, thereby facilitating electrical measurements. Pure $BiFeO_3$ films were also prepared in this study.

Coatings from the $BiFeO_3$ precursor solution were deposited on rigid $Pt/TiO_2/SiO_2/(100)Si$ (Radiant Technologies Inc.) and flexible Pt/NiCr/PI/NiCr/Pt (75 μm thick UPILEX-S polyimide – PI, UBE Industries Ltd) substrates by spin-coating (2000 rpm for 45 s) or dip-coating (draw speed of 150 mm per minute). The solution layers were dried at 100 °C for 5 minutes on a hot plate. For the processing of the metal oxide films, the dried layers were placed in a hermetically sealed, laboratory-scale reactor equipped with a high-intensity excimer lamp. A PhotoLabXe2 excimer system with an emission wavelength of 172 nm, an irradiation area of approximately 52 cm^2, and an irradiance of approximately 20 mW cm^{-2} was used for this process, with the lamp positioned 2 cm from the sample. Although time dependent variations in the effective UV irradiance inside the sealed treatment chamber cannot be completely excluded, the irradiation geometry and atmospheric conditions were kept strictly constant throughout all experiments. This ensured reproducible operation, as demonstrated by the results presented in this work and by the continued and consistent performance of this experimental setup over extended use. This reactor was designed to allow the introduction of different types of gases. Gentle heating of the films below 250 °C was achieved using commercial hot-plate ceramic heaters (ULTRAMIC Advanced Ceramic Heaters). A flowing O_2 was used to carry out a controlled water vapor atmosphere inside the chamber. This atmosphere was created by passing high purity oxygen through deionized water and subsequently introducing this humidified gas flow into the irradiation chamber. Water condensation inside the irradiation chamber, and consequently on the film surface, was avoided by maintaining the chamber temperature at approximately 40 °C using a heating blanket. The relative humidity was monitored using a thermohygrometer (Vaisala Humicap HM41), which was installed at the outlet of the gas flow under dynamic conditions. Specifically, the sensor was inserted into a sealed flask out of the irradiation chamber, which is equipped with two ports: one connected to the gas outlet from the irradiation chamber and the other directing the exhaust gas to the laboratory ventilation system. Once a relative humidity above 80% was reached, the gas outlet of the irradiation chamber was closed in order to maintain a static, water vapour enriched atmosphere inside the chamber. At this point, the UV lamp was switched on, generating an atmosphere rich in hydroxyl (•OH) radicals inside the irradiation chamber while the film was heated at 150 °C for 30 min using the commercial ULTRAMIC ceramic hot plate equipped with an internal thermocouple to control the heater temperature. The temperature of the film surface was independently monitored using a second thermocouple placed directly on the film surface. During these initial 30 min, an •OH radical rich atmosphere was generated inside the irradiation chamber using the 172 nm UV excimer lamp through the reactions occurring in the humid irradiation atmosphere. These reactions are described in detail in Fig. 1 and in the SI (Fig. S3). After the initial 30 min treatment of the film under the •OH radical rich atmosphere, the atmosphere inside the irradiation chamber was replaced by pure O_2. This was achieved by introducing a flow of pure oxygen into the chamber for 10 min while opening the gas outlet, thereby flushing out the •OH rich atmosphere. Subsequently, the gas outlet was closed, maintaining a static pure O_2 atmosphere inside the chamber. Under irradiation with the 172 nm UV lamp, this O_2 atmosphere led to the generation of ozone (O_3) according to the reactions indicated in Fig. 1 and in the SI (Fig. S3). The film, maintained at 150 °C, was further treated under this highly oxidizing O_3 atmosphere for 30 min. Subsequently, the annealing temperature was increased to 250 °C, and the film was kept at this temperature for an additional 30 min inside the irradiation chamber under 172 nm UV irradiation. The entire film processing was carried out using a computer controlled system integrated with the irradiation chamber, allowing safe and reproducible operation. Dedicated measurement and control software was developed based on the Eurotherm system to regulate temperatures and processing times inside the irradiation chamber during treatment with the 172 nm UV lamp. The resulting films were then annealed in O_2 at low temperatures using rapid heating rates (3 °C s^{-1} and 30 °C s^{-1}). The real-time temperature of the film during thermal treatment was monitored by the internal controllers of the equipment (thermocouple and pyrometer), as well as with an external thermocouple placed on the film surface. The novel process, designed in this work to induce chemical reactions in the solution-deposited film under •OH radical-rich atmospheres, is detailed at the bottom of Fig. S1. To help determine the synthesis mechanisms developed during the UV-irradiation process under a gaseous •OH radical atmosphere, the solution-deposited films were also subjected to conventional fabrication processes. In these cases, the films were processed in the same way, but without UV irradiation and under atmospheres of air or H_2O vapor.

Electron Paramagnetic Resonance (EPR) experiments were conducted using two different spin-trapping agents: 2,2,6,6-tetramethylpiperidine 1-oxyl (TEMPO) and 5,5-dimethyl-1-pyrroline *N*-oxide (DMPO). These agents were introduced into a hermetically sealed chamber saturated with water vapor and exposed to UV irradiation to generate an atmosphere enriched with hydroxyl (•OH) radicals.

For sample preparation, 300 μL of aqueous or ethanol-dried solutions of TEMPO or DMPO ($\sim$0.2 mol L^{-1}) were placed in flat alumina crucibles to maximize the surface area exposed to the reactive atmosphere. The samples were then incubated in a hydroxyl radical (•OH)-enriched environment for 30 minutes at room temperature. Following incubation, the solutions were diluted to approximately 500 μL prior to electron spin resonance (EPR) analysis. All the EPR spectra were recorded at room temperature with a Bruker EMX-12 spectrometer operating at the X-band, with a modulation frequency of 100 kHz and an amplitude of 0.1 mT.

The steps of the fabrication process of the hydroxyl ($^{\bullet}$OH) radical-assisted processing method designed by our group (Fig. S2) to achieve metal oxide film crystallization at low temperatures is schematically shown in Fig. S3.

Infrared Reflection Absorption Spectroscopy (IRRAS) analysis was performed using a Bruker IFS 66V-S on films deposited on commercial Pt-coated (100)Si substrates ($Pt/TiO_2/SiO_2/(100)Si$) with thicknesses below 100 nm. This analysis was carried out on solution-deposited films processed in atmospheres containing UV-generated $^{\bullet}$OH radicals, as well as on solution-deposited films subjected to the as referred as conventional fabrication processes (without UV irradiation) in air and H_2O vapor atmospheres. The evolution of all vibrational modes recorded in the IRRAS spectra was studied by calculating the integrated areas of these bands. The normalized areas were plotted as a function of the processing steps, with each step associated with a discrete parameter on the *x*-axis. The data from these plots (Fig. S4) for each vibrational mode were fitted to the mathematical functions that best matched, considering the chemical significance of such fittings.

Fourier Transform Infrared Spectroscopy (FTIR) was employed to investigate the wavelength range in which metal–nitrogen bonds are typically detected (below 200 cm^{-1}). Therefore, measurements were performed using a Bruker IFS 66V-S spectrometer over the wavelength range of 1000 cm^{-1} to 50 cm^{-1}, exclusively for the bismuth precursor. This approach allows differentiation between the Bi–N bond, which appears between 50 cm^{-1} and 200 cm^{-1}, and the Bi–O bond, which appears between 200 cm^{-1} and 1000 cm^{-1}. Directly deposited films on substrates were not suitable for this analysis due to interference from the substrate. Therefore, FTIR measurements were performed on pellets prepared from the gel samples obtained after treatment in the sealed chamber, mixed with polyethylene $(C_2H_4)_n$, which does not absorb in this spectral region. For this study, gel samples were prepared by placing 300 μL of the solution into a flat alumina crucible to maximize the surface area exposed to the reactive atmosphere. The crucible with the sample was then placed in a sealed chamber and subjected to the various processing conditions investigated in this study.

Electrospray Ionization Mass Spectrometry (ESI-MS) and Atmospheric Pressure Chemical Ionization Mass Spectrometry (APCI-MS), both operated in positive mode with a source voltage of +5.5 kV, were employed to analyze the bismuth and iron precursors resulting from their processing in the atmosphere of UV-generated $^{\bullet}$OH radicals. The analyses were performed using a Bruker MAXIS II instrument, offering a mass range of 20–40 000 Da and a resolution of 80 000 at *m/z* 1222. This system is connected to a Bruker ULTRAFLEX III mass spectrometer (MALDI-TOF/TOF), which has a mass range up to 150 000 Da and a resolution of 20 000 FWHM. Aliquots of the precursor solutions were diluted in either acetonitrile (C_2H_3N) or dichloromethane (CH_2Cl_2) prior to measurement.

The crystalline phases developed in the films were monitored by XRD (D8 ADVANCE instrument, Cu Kα radiation, Bruker), using Bragg–Brentano geometry and an incident beam wavelength of $\lambda_{CuK\alpha}$ = 1.5418 Å. Field Emission Gun Scanning Electron Microscopy (FEG-SEM) was used to observe the surface morphology of the films (Nova NanoSEM 230 instrument, FEI Company). Cross-sectional samples of the films on PI were prepared by fracturing them in liquid nitrogen.

To demonstrate the functionality of these films, planar arrays of capacitors were fabricated by evaporating top Pt electrodes onto the $BiFeO_3$ film surface through a shadow mask (with a diameter of ∼200 μm and a thickness of ∼10 nm). These films were grown on rigid $Pt/TiO_2/SiO_2/(100)Si$ and flexible Pt/NiCr/PI/NiCr/Pt substrates, with thicknesses between 100 nm and 200 nm, where the metal coating on the substrates served as the bottom electrode for the capacitors. The functional response was tested by measuring the ferroelectric and pyroelectric responses of these capacitors. Current density *vs.* electric field (*J–E*) curves were measured at room temperature (@RT) under sine waves with frequencies between 1 and 5 kHz, applied using an HP 8116A function generator. The generated currents were amplified with a Keithley 428 current amplifier and collected using a Tektronix (TDS 520) oscilloscope. Ferroelectric hysteresis loops were obtained by integrating the *J–E* curves.

Magnetic field (*M–H*) hysteresis loops were measured at 4.2 K and @RT (300 K) using a superconducting quantum interference device (SQUID) magnetometer (Quantum Design) equipped with a 5-Tesla coil. The magnetic field was applied parallel to the film surface. To isolate the intrinsic magnetic response of the films, the diamagnetic contribution from the substrate was subtracted by fitting the high-field region of the data to a linear baseline with a negative slope. These measurements were performed on $BiFeO_3$ perovskite films deposited on both rigid Pt-coated Si and flexible polyimide (PI) substrates. The films were fabricated using the novel $^{\bullet}$OH radical-assisted film solution synthesis platform developed in this work.

The biocompatibility *in vitro* of the flexible materials was evaluated using the established cell line of L929 mouse fibroblasts. Three rectangular material pieces (3 mm × 3 mm) were cut for each experimental series: pristine PI, metallized PI with NiCr and with NiCr and Pt coatings (the commonly used electrode in the fabrication of capacitor devices on polyimide (PI) substrates), and $BiFeO_3$ on the metallized PI substrate (PI, NiCr/PI, Pt/NiCr/PI and the $BiFeO_3$/Pt/NiCr/PI). These material pieces were sterilized under UV irradiation in a safety cabinet for 30 minutes. Cells were seeded in a 24-well culture plate at a density of 1×10^4 cells per well (cell count performed in a Neubauer chamber) in 1 mL of culture medium (basal medium (DMEM) + 10% fetal bovine serum (FBS) + penicillin/streptomycin + GlutaMAX), and maintained in a cell incubator under CO_2 atmosphere (5%) at 37 °C for 7 days. The morphology and density of the cultures at the periphery of the substrates were monitored using an inverted optical microscope with an attached digital camera. Cell viability was analyzed by using the Live/Dead Viability kit (Invitrogen). This kit is based on the use of calcein and ethidium homodimer-1 (EthD-1). After staining, the samples were visualized using a confocal laser scanning microscope SP5 (Leica). To quantify cell viability, the

percentage area ($N \geq 3$) of live (green) and dead (red) cells was calculated from the acquired microscopy images. Cell morphology of the cultures in the different substrates were also studied by scanning electron microscopy (SEM). Samples were fixed in 2.5% glutaraldehyde (in distilled water) for 45 minutes at room temperature, followed by dehydration through a graded ethanol series (30%, 50%, 70%, 90%, and 100%), with each step performed twice for 15 min. After complete drying, samples were mounted on metal stubs using carbon tape, coated with a thin layer of gold (*ca.* 10 nm), and imaged using a FEI VERIOS 460 scanning electron microscope. Glass coverslips were functionalized following the same protocol as for the previous substrates and used as control substrates in all *in vitro* studies.

The general applicability of this selective gaseous $^{\bullet}OH$ radical photochemical synthesis method for enhancing the crystallization of metal oxide films has also been demonstrated in this work for thin films of solid solutions of multiple oxides such as the ferroelectric $BiFeO_3$ and $Pb(Zr_xTi_{1-x})O_3$ (PZT) perovskites and for single oxides such as TiO_2 and Bi_2O_3. The demonstration of the reduction of the activation energy (E_a) for the crystallization of metal oxide films by using this processing method, was evaluated in single metal oxide films of TiO_2 (anatase). The overall activation energy (E_a) for the crystallization of these TiO_2 films was semiquantitative calculated using data from X-ray diffraction (XRD) and Avrami plots.

To highlight the broad applicability of this processing method across a wide range of metal oxide compositions, irrespective of the specific metal precursor or solution chemistry, TiO_2 films were deposited from precursor solutions containing a modified titanium alkoxide, specifically titanium diisopropoxide bis-acetylacetonate ($Ti(OCH(CH_3)_2)_2(CH_3COCHCOCH_3)_2$). Bi_2O_3 films were prepared from precursor solutions containing the Bi-*mdea* complex. For the PZT films, the precursor solutions were formulated using lead acetate trihydrate ($Pb(CH_3COO)_2 \cdot 3H_2O$) as the lead source, zirconium tetraisopropoxide ($Zr(OCH(CH_3)_2)_4$) partially stabilized with acetylacetone ($CH_3COCH_2COCH_3$) as the zirconium source, and titanium diisopropoxide bis-acetylacetonate as the titanium source.

Author contributions

Y. A. R. conducted the experimental work related to the synthesis of the solutions and the solution deposition of $BiFeO_3$ films, contributing also to the physico-chemical characterization of the precursors, as well as to the structural and microstructural characterization of the films. J. A. M-C. analyzed the evolution of the integrated areas of the vibrational modes recorded by IRRAS, associated with the different chemical bonds present or formed in the system, fitting also the experimental curves to mathematically coherent functions from a physico-chemical perspective. A. B. performed the experimental characterization of the functional properties of $BiFeO_3$ films and contributed to the discussion of the data in relation to the processing. M. E.-C. carried out the experimental work involving the solution deposition of single-oxide TiO_2 films and investigated their crystallization kinetics under various processing conditions, contributing also to the study of $BiFeO_3$ films. J. A. V.-M. performed the Electron Paramagnetic Resonance (EPR) analysis of the samples and contributed to the interpretation and discussion of the results. M. C. S. performed and supervised the biocompatibility experiments on the flexible materials, contributed to the analysis and discussion of the results and reviewed the final version. R. J. supervised the functional characterization of $BiFeO_3$ films and was responsible for analyzing, discussing, and writing the section related to the functional response of the films. Í. B. supervised the experimental work related to the solution deposition of the films, reviewed successive drafts of the manuscript leading to the final version, and contributed to funding acquisition for this research line. M. L. C. conceptualized the research, supervised the experimental work, contributed to funding acquisition, wrote the original draft of the manuscript, and revised its successive versions leading to the final version presented here.

Conflicts of interest

There are no conflicts to declare.

Data availability

The supporting data are provided as part of the supplementary information (SI). Supplementary information is available. See DOI: https://doi.org/10.1039/d6tc00519e.

Additional information can be requested directly from the corresponding author.

Acknowledgements

This work was supported by the Spanish projects PID2022-136790OB-I00, PID2021, CNS2022-135743 and TED2021-130871BC21 funded by MCIN/AEI/10.13039/501100011033 and the European Union through the ''NextGeneration EU''/PRTR initiative. The Severo Ochoa Centres of Excellence program is acknowledged through Grant CEX2024-001445-S. A. B acknowledges financial support of the CAM PhD grant from the Comunidad de Madrid (PIPF-2024ECO-33982). The authors acknowledge Teresa Blasco Ibáñez for contributing to the interpretation and discussion of the Electron Paramagnetic Resonance (EPR) results of the samples obtained at the Instituto de Tecnología Química (UPV-CSIC), Universitat Politècnica de Valencia – Consejo Superior de Investigaciones Científicas. The Advanced Light Microscopy Service at the *Centro Nacional de Biotecnología* (CNB–CSIC) is acknowledged for assistance with confocal microscopy studies. The Scanning Electron Microscopy Service at the Instituto de Micro y Nanotecnología (IMN-CSIC) is acknowledged for support with SEM studies. The MiNa Laboratory at IMN acknowledges its funding from CM (project S2018/NMT-4291 TEC2SPACE), MINECO (project CSIC13-4E-1794), and EU (FEDER, FSE)''.

References

1 J. W. Park, B. H. Kang and H. J. Kim, A Review of Low-Temperature Solution-Processed Metal Oxide Thin-Film Transistors for Flexible Electronics, *Adv. Funct. Mater.*, 2020, **30**, 1904632, DOI: 10.1002/adfm.201904632.

2 S. A. Delbari, L. S. Ghadimi, R. Hadi, S. Farhoudian, M. Nedaei, A. Babapoor, A. S. Namini, Q. Van Le, M. Shokouhimehr, M. S. Asl and M. Mohammadi, Transition metal oxide-based electrode materials for flexible supercapacitors: A review, *J. Alloys Compd.*, 2021, **857**, 158281, DOI: 10.1016/j.jallcom.2020.158281.

3 J. Wiklund, A. Karakoç, T. Palko, H. Yigitler, K. Ruttik, R. Jäntti and J. Paltakari, A review on printed electronics: fabrication methods, inks, substrates, applications and environmental impacts, *J. Manuf. Mater. Process*, 2021, **5**, 89, DOI: 10.3390/jmmp5030089.

4 A. Sudheshwar, N. Malinverno, R. Hischier, B. Nowack and C. Som, The need for design-for-recycling of paper-based printed electronics – a prospective comparison with printed circuit boards, *Resour. Conserv. Recycl.*, 2023, **189**, 106755, DOI: 10.1016/j.resconrec.2022.106757.

5 EU Commission GREENDEAL, https://commission.europa.eu/strategy-and-policy/priorities-2019-2024/european-green-deal.

6 E. Carlos, R. Branquinho, R. Martins and E. Fortunato, New challenges of printed high-κ oxide dielectrics, *Solid-State Electron.*, 2021, **183**, 108044, DOI: 10.1016/j.sse.2021.108044.

7 L. Song, J. Cardoletti, A. Blázquez Martínez, A. Benčam, B. Kmet, S. Girod, E. Defay and S. Glinšek, Crystallization of piezoelectric films on glass via flash lamp annealing, *Nat. Commun.*, 2024, **15**, 1890, DOI: 10.1038/s41467-024-46257-0.

8 H. J. Kim, Y. An, Y. C. Jung, J. Mohan, J. G. Yoo, Y. I. Kim, H. Hernandez-Arriaga, H. S. Kim, J. Kim and S. J. Kim, Low-Thermal-Budget Fluorite-Structure Ferroelectrics for Future Electronic Device Applications, *Phys. Status Solidi RRL*, 2021, **15**, 2100028, DOI: 10.1002/pssr.202100028.

9 L. Song, S. Glinsek and E. Defay, Toward low-temperature processing of lead zirconate titanate thin films: Advances, strategies, and applications, *Appl. Phys. Rev.*, 2021, **8**, 041315, DOI: 10.1063/5.0054004.

10 Y.-R. Jo, W.-J. Lee, M.-H. Yoon and B.-J. Kim, In Situ Tracking of Low-Temperature VO_2 Crystallization via Photocombustion and Characterization of Phase-Transition Reliability on Large-Area Flexible Substrates, *Chem. Mater.*, 2020, **32**, 4013–4023, DOI: 10.1021/acs.chemmater.0c00581.

11 I. Bretos, R. Jiménez, J. Ricote and M. L. Calzada, Low-Temperature Solution Approaches for the Potential Integration of Ferroelectric Oxide Films in Flexible Electronics, *IEEE Trans. Ultrason. Eng.*, 2020, **67**(10), 1967–1979, DOI: 10.1109/TUFFC.2020.2995287.

12 E. Carlos, R. Branquinho, R. Martins, A. Kiazadeh and E. Fortunato, Recent Progress in Solution-Based Metal Oxide Resistive Switching Devices, *Adv. Mater.*, 2021, **33**, 2004328, DOI: 10.1002/adma.202004328.

13 I. Bretos, R. Jiménez, J. Ricote and M. L. Calzada, Low temperature crystallization of solution-derived metal oxide thin films assisted by chemical processes, *Chem. Soc. Rev.*, 2018, **47**, 291–308, DOI: 10.1039/C6CS00917D.

14 M. L. Calzada, Sol–Gel Electroceramic Thin Films, in *The Sol–Gel Handbook: Synthesis, Characterization, and Applications*, ed. D. Levy and M. Zayat, Wiley-VCH Verlag GmbH & Co. KGaA, 2015, ch. 27, vol. 2, pp. 841–880.

15 S. Lee, S. H. Lee, N. On and J. K. Jeong, A solution processed La–Zr–O dielectric at a low temperature for high-performance In-Ga-O transistors: Engineering a precursor solution, *Ceram. Int.*, 2021, **47**, 6918–6927, DOI: 10.1016/j.ceramint.2020.11.038.

16 M.-H. Jao, C.-C. Cheng, C.-F. Lu, K.-C. Hsiao and W.-F. Su, Low temperature and rapid formation of high quality metal oxide thin film via a hydroxide assisted energy conservation strategy, *J. Mater. Chem. C*, 2018, **6**, 9941–9949, DOI: 10.1039/C8TC03544J.

17 K. K. Banger, Y. Yamashita, K. Mori, R. L. Peterson, T. Leedham, J. Rickard and H. Sirringhaus, Low-temperature, high-performance solution-processed metal oxide thin-film transistors formed by a 'sol–gel on chip' process, *Nat. Mater.*, 2011, **10**, 45–50, DOI: 10.1038/nmat2914.

18 G. Feng, P. Cheng, W. Yan, M. Boronat, X. Li, J.-H. Su, J. Wang, Y. Li, A. Corma, R. Xu and J. Yu, Accelerated crystallization of zeolites via hydroxyl free radicals, *Science*, 2016, **351**, 62781188, DOI: 10.1126/science.aaf1559.

19 S. Park, K.-H. Kim, J.-W. Jo, S. Sung, K.-T. Kim, W.-J. Lee, J. Kim, H. J. Kim, G.-R. Yi, Y.-H. Kim, M.-H. Yoon and S. K. Park, In-Depth Studies on Rapid Photochemical Activation of Various Sol–Gel Metal Oxide Films for Flexible Transparent Electronics, *Adv. Funct. Mater.*, 2015, **25**, 2807–2815, DOI: 10.1002/adfm.201500545.

20 A. Gómez-Lopez, Y. A. Rivas, S. López-Fajardo, R. Jiménez, J. Ricote, C. Pecharromán, I. Montero, I. Bretos and M. L. Calzada, *In situ* photogenerated hydroxyl radicals in the reaction atmosphere for the accelerated crystallization of solution-processed functional metal oxide thin films, *J. Mater. Chem. C*, 2023, **11**, 2619–2629, DOI: 10.1039/d2tc05447g.

21 I. Bretos, R. Jiménez, J. Ricote and M. L. Calzada, Photochemistry in the Low-Temperature Processing of Metal Oxide Thin Films by Solution Methods, *Chem. – Eur. J.*, 2020, **26**, 9277–9291, DOI: 10.1002/chem.202000244.

22 Y.-H. Kim, J.-S. Heo, T.-H. Kim, S. Park, M.-H. Yoon, J. Kim, M. S. Oh, G.-R. Yi, Y.-Y. Noh and S. K. Park, Flexible metal oxide devices made by room-temperature photochemical activation of sol–gel films, *Nature*, 2012, **489**, 128–191, DOI: 10.1038/nature11434.

23 M. L. Calzada, I. Bretos, R. Jiménez, J. Ricote, R. Sirera, M. Algueró, A. Barreto, Y. A. Rivas. and M. Echániz-Cíntora, Solution-deposited ferroelectric BiFeO3 perovskite-based films. A spotlight on their manifold applications in emerging technologies, *ACS Appl. Energy Mater.*, 2025, **8**, 2845–2868, DOI: 10.1021/acsaem.4c02906.

24 K. Makino, A. Hagi, H. Ide, A. Murakami and M. Nishi, Mechanistic studies on the formation of aminoxyl radicals from 5,5-dimethyl-1-pyrroline-*N*-oxide in Fenton systems. Characterization of key precursors giving rise to background ESR signals, *Can. J. Chem.*, 1992, **70**(11), 2818–2827, DOI: 10.1139/v92-358.

25 A. Bosnjakovic and S. Schlick, Spin Trapping by 5,5-Dimethylpyrroline-N-oxide in Fenton Media in the Presence of Nafion Perfluorinated Membranes: Limitations and Potential, *J. Phys. Chem. B*, 2006, **110**(22), 10720–10728, DOI: 10.1021/jp061042y.

26 J. M. Fontmorin, R. C. Burgos Castillo, W. Z. Tang and M. Sillanpää, Stability of 5,5-dimethyl-1-pyrroline-N-oxide as a spin-trap for quantification of hydroxyl radicals in processes based on Fenton reaction, *Water Res.*, 2016, **99**, 24–32, DOI: 10.1016/j.watres.2016.04.053.

27 L. Fabbrizzi, Beauty in Chemistry: Making artistic molecules with Schiff Bases, *J. Org. Chem.*, 2020, **85**, 12212–12226, DOI: 10.1021/acs.joc.0c01420.

28 S. Krompiec, M. Krompiec, R. Penczek and H. Ignasiak, Double bond migration in N-alytic systems catalyzed by transition metal complexes, *Coord. Chem. Rev.*, 2008, **252**, 1819–1841, DOI: 10.1016/j.ccr.2007.12.013.

29 K. Bakken, V. H. Pedersen, A. B. Blichfeld, I. E. Nylund, S. Tominaka, K. Ohara, T. Grande and M. A. Einarsrud, Structures and Role of the Intermediate Phases on the Crystallization of $BaTiO_3$ from an Aqueous Synthesis Route, *ACS Omega*, 2021, **6**, 9567–9576, DOI: 10.1021/acsomega.1c00089.

30 P. Hermet, M. Goffinet, J. Kreisel and P. Ghosez, Raman and infrared spectra of multiferroic bismuth ferrite from first principles, *Phys. Rev. B: Condens. Matter Mater. Phys.*, 2007, **75**, 220102(R), DOI: 10.1103/PhysRevB.75.220102.

31 D. Pérez-Mezcua, R. Sirera, R. Jiménez, I. Bretos, C. De Dobbelaere, A. Hardy, M. K. Van Bael, M. L. Calzada and A. UV-absorber, bismuth(III)-N-methyldiethanolamine complexes for bismuth-based oxide thin films, *J. Mater. Chem. C*, 2014, **2**(41), 8750–8760, DOI: 10.1039/c4tc00960f.

32 S. Mishra and S. Daniele, Molecular engineering of metal alkoxides for solution phase synthesis of high-tech metal oxide nanomaterials, *Chem. – Eur. J.*, 2020, **26**, 9292–9303, DOI: 10.1002/chem.202000534.

33 I. Bretos, R. Jiménez, J. Ricote, R. Sirera and M. L. Calzada, Photoferroelectric thin films for flexible systems by a Three-in-One solution-based approach, *Adv. Funct. Mater.*, 2020, **30**(32), 2001897, DOI: 10.1002/adfm.202001897.

34 R. K. Sodhi and S. Pau, An overview of metal acetylacetonates: Developing Areas/Routes to New Materials and Applications in Organic Synthesis, *Catal. Surv. Asia*, 2018, **22**, 31–62, DOI: 10.1007/s10563-017-9239-9.

35 P. Brophy and D. K. Farmer, Clustering, methodology, and mechanistic insights into acetate chemical ionization using high-resolution time-of-flight mass spectrometry, *Atmos. Meas. Tech.*, 2016, **9**, 3969–3986, DOI: 10.5194/amt-9-3969-2016.

36 C. Gutierrez-Lazaro, I. Bretos, R. Jimenez, J. Ricote, H. El Hosiny, D. Perez-Mezcua, R. J. Jimenez Rioboó, M. Garcıa-Hernández and M. L. Calzada, Solution Synthesis of $BiFeO_3$ Thin Films onto Silicon Substrates with Ferroelectric, Magnetic, and Optical Functionalities, *J. Am. Ceram. Soc.*, 2013, **96**(10), 3061–3069, DOI: 10.1111/jace.12569.

37 International Roadmap for Devices and Systems (IRDS™) 2023 Update, https://irds.ieee.org/editions/2023.

38 C. De Dobbelaere, M. L. Calzada, R. Jiménez, J. Ricote, I. Bretos, J. Mullens, A. Hardy and M. K. Van Bael, Aqueous Solutions for Low-Temperature Photoannealing of Functional Oxide Films: Reaching the 400 °C Si-Technology Integration Barrier, *J. Am. Ceram. Soc.*, 2011, **133**, 12922–12925, DOI: 10.1021/ja203553n.

39 M. Algueró, M. L. Calzada, L. Pardo and E. Snoeck, Combined effect of grain size and tensile stresses on the ferroelectric properties of sol-gel (Pb,La)TiO_3 thin films, *J. Mater. Res.*, 1999, **14**(12), 4570–4580, DOI: 10.1557/JMR.1999.0619.

40 L. San-Miguel, A. Castellanos-Aliaga, R. Codrón, D. G. Calatayud, A. Caballero, C. Gumiel, A. C. Caballero, T. Jardiel and M. Peiteado, Substrate-film interfacial interaction in the fabrication of ZnO photocatalytic thin films via sol-gel and aqueous solution-gel CSD processing, *Ceram. Int.*, 2025, **51**(25), 46865–46878, DOI: 10.1016/j.ceramint.2025.07.391.

41 I. Bretos, R. Jiménez, M. Tomczyk, E. Rodríguez-Castellón, P. M. Vilarinho and M. L. Calzada, Active layers of high performance lead zirconate titanate at low temperatures compatible with silicon nano- and miroelectronic devices, *Sci. Rep.*, 2016, **6**, 20143.

42 A. Domínguez-Bajo, J. M. Rosa, A. González-Mayorga, B. L. Rodilla, A. Arché-Núñez, E. Benayas, P. Ocón, L. Pérez, J. Camarero, R. Miranda, M. T. González, J. Aguilar, E. López-Dolado and M. C. Serrano, Nanostructured gold electrodes promote neural maturation and network connectivity, *Biomaterials*, 2021, **279**, 121186, DOI: 10.1016/j.biomaterials.2021.121186.

